BOOMERanG constraints on primordial non-Gaussianity from analytical Minkowski functionals

Mon. Not. R. Astron. Soc. **000**, 000–000 (0000) Printed 9 August 2011 (MN LATEX style file v2.2)

BOOMERanG Constraints on Primordial Non-Gaussianity from Analytical Minkowski Functionals

P. Natoli[1,2⋆], G. De Troia[1], C. Hikage[3,4], E. Komatsu[5], M. Migliaccio[1], P. A. R. Ade[4], J. J. Bock[6], J. R. Bond[7], J. Borrill[8,9], A. Boscaleri[10], C. R. Contaldi[11], B. P. Crill[6], P. de Bernardis[12], G. de Gasperis[1], A. de Oliveira-Costa[13], G. Di Stefano[14], E. Hivon[15], T. S. Kisner[8,9], W. C. Jones[16], A. E. Lange[17], S. Masi[12], P. D. Mauskopf[4], C. J. MacTavish[18], A. Melchiorri[12,19], T. E. Montroy[20], C. B. Netterfield[21], E. Pascale[21], F. Piacentini[12], G. Polenta[12,22,23], S. Ricciardi[8,9], G. Romeo[14], J. E. Ruhl[20], M. Tegmark[13], M. Veneziani[12] and N. Vittorio[1]

[1] *Dipartimento di Fisica, Università di Roma "Tor Vergata", Via della Ricerca Scientifica, 1 I-00133 Roma, Italy*
[2] *INFN, Sezione di Tor Vergata, Roma, Italy*
[3] *Department of Astrophysical Sciences, Princeton University, Peyton Hall, Princeton NJ 08544, USA*
[4] *School of Physics and Astronomy, Cardiff University, Cardiff, CF24 3AA*
[5] *Texas Cosmology Center, University of Texas at Austin, 1 University Station, C1400, Austin, TX 78712, USA*
[6] *Jet Propulsion Laboratory, Pasadena, CA, USA*
[7] *Canadian Institute for Theoretical Astrophysics, University of Toronto, Toronto, Ontario, Canada*
[8] *Computational Research Division, Lawrence Berkeley National Laboratory, Berkeley, CA, USA*
[9] *Space Sciences Laboratory, UC Berkeley, CA, USA*
[10] *IFAC-CNR, Firenze, Italy*
[11] *Theoretical Physics Group, Imperial College, London*
[12] *Dipartimento di Fisica, Università La Sapienza, Roma, Italy*
[13] *Department of Physics, MIT, Cambridge, MA 02139, USA*
[14] *Istituto Nazionale di Geofisica e Vulcanologia, 00143 Rome, Italy*
[15] *Institut d'Astrophysique, Paris, France*
[16] *Department of Physics, Princeton University, Princeton, NJ 0854, USA*
[17] *Observational Cosmology, California Institute of Technology, Pasadena, CA, USA*
[18] *Astrophysics Group, Imperial College, London*
[19] *INFN, Sezione di Roma 1, Roma, Italy*
[20] *Physics Department, Case Western Reserve University, Cleveland, OH, USA*
[21] *Physics Department, University of Toronto, Toronto, Ontario, Canada*
[22] *ASI Science Data Center, c/o ESRIN, 00044 Frascati, Italy*
[23] *INAF - Osservatorio Astronomico di Roma, Monte Porzio Catone, Italy*

9 August 2011

ABSTRACT

We use Minkowski Functionals (MF) to constrain a primordial non-Gaussian contribution to the CMB intensity field as observed in the 150 GHz and 145 GHz BOOMERanG maps from the 1998 and 2003 flights, respectively, performing for the first time a joint analysis of the two datasets. A perturbative expansion of the MF formulae in the limit of a weakly non-Gaussian field yields analytical formulae, derived by Hikage et al. (2006), which can be used to constrain the coupling parameter $f_{\rm NL}$ without the need for non-Gaussian simulations. We find $-1020 < f_{\rm NL} < 390$ at 95% CL, significantly improving the previous constraints by De Troia et al. (2007) on the BOOMERanG 2003 dataset. These are the best $f_{\rm NL}$ limits to date for suborbital probes.

Key words: Cosmology: early Universe – cosmic microwave background – methods: statistical – analytical

1 INTRODUCTION

Detection of non-Gaussian signals in the Cosmic Microwave Background anisotropy pattern can be of significant help in discriminating between different inflationary models. The most simple inflationary models based on single-rolling scalar fields predict very small deviations from Gaussianity that cannot be usefully constrained by present day experimental efforts (Bartolo et al. 2004). However, multi-field inflationary models and other alternative scenarios allow for more relevant non-Gaussian contribution that could be in principle detected by current and forthcoming missions (Bernardeau & Uzan 2002; Lyth et al. 2003). In this paper we consider only the so-called local form for primordial non-Gaussianity, which can be parametrized by means of a quadratic term in Bardeen's curvature perturbations Φ (Salopek & Bond 1990; Gangui et al. 1994; Verde et al. 2000; Komatsu & Spergel 2001):

$$\Phi(\mathbf{x}) = \Phi_G(\mathbf{x}) + f_{\rm NL}\left[\Phi_G(\mathbf{x})^2 - \left\langle \Phi_G(\mathbf{x})^2 \right\rangle\right], \qquad (1)$$

where Φ_G is a zero mean, Gaussian random field and $f_{\rm NL}$ is the coupling parameter that characterizes the amplitude of primordial non-Gaussianity. At present, the most stringent limits on $f_{\rm NL}$ are derived from the WMAP five year analysis at $-4 < f_{\rm NL} < 80$ (95% CL) using an optimal (i.e. minimum-variance) bispectrum based estimator (Smith et al. 2009). Many teams have further analysed the WMAP dataset to yield constraints on $f_{\rm NL}$ using a plethora of tests, including wavelet based estimators: see e.g. Curto et al. (2009); Rudjord et al. (2009); Pietrobon et al. (2009) and references therein. All $f_{\rm NL}$ limits to date are compatible with a Gaussian hypothesis. Yadav & Wandelt (2008) claimed a measure of a positive $f_{\rm NL}$ at above 99.5% CL in the WMAP three-year data using a bispectrum based statistics; however, their claimed signal has not been confirmed by the WMAP five-year analysis (Komatsu et al. 2008; Smith et al. 2009).

On the other hand, several groups have also investigated specific signatures in the WMAP data, typically induced by low resolution features such as anomalous spots, reporting high significance yet unmodelled detection of non-Gaussianity (Creminelli et al. 2007; Cruz et al. 2007; Vielva et al. 2004; Eriksen et al. 2007; Park et al. 2007; Räth et al. 2009).

CMB suborbital experiments have also delivered $f_{\rm NL}$ constraints, particularly MAXIMA (Santos et al. 2003), VSA (Smith et al. 2004), BOOMERanG (De Troia et al. 2007) and ARCHEOPS (Curto et al. 2008). Although such limits are weaker than those based on WMAP, they probe a range of angular scale that will not be accessible to space borne observation until the advent of Planck [1]. Among suborbital probes, De Troia et al. (2007) set the most stringent $f_{\rm NL}$ constraints to date at $-800 < f_{\rm NL} < 1050$ (95% CL) from BOOMERanG 2003 (hereafter B03) dataset using a pixel space statistics based on Minkowski functionals. Such constraints were obtained using a reference Monte Carlo set composed of non-Gaussian CMB maps.

In this paper we revisit the $f_{\rm NL}$ analysis of the BOOMERanG dataset. We employ a larger dataset that also includes the BOOMERanG 1998 (hereafter B98) data, allowing for a larger sky coverage and improved signal to noise. Furthermore, we apply a different, harmonic based, Minkowski functional code that overcomes a weakness of the previous B03 analysis, which used a flat sky approximation to compute the functionals. Finally, we employ the perturbative approach developed by Hikage et al. (2006) to quantify the contribution of primordial non-Gaussianity to MF. Hikage et al. (2008) successfully applied the perturbative method to WMAP data without need of a large set of non-Gaussian simulations.

The plan of this paper is as follows. In Section 2 we briefly describe the BOOMERanG experiment and the two datasets it has produced as well as our data analysis pipeline. In Section 3 we apply the perturbative formulae to compute the MFs of the data and Gaussian Monte Carlo simulation maps. Furthermore in Section 4 we constrain $f_{\rm NL}$ and in section 5 we draw our main conclusions.

2 THE B98 AND B03 DATASETS

BOOMERanG was launched for the first time from Antarctica in December 1998. It has observed the sky for about 10 days, centering a target region at RA $\sim 5h$ and DEC $\sim -45^\circ$ that is free of contamination by thermal emission from interstellar dust. BOOMERanG mapped this region scanning the telescope through 60° at fixed elevation and at constant speed. At intervals of a few hours the telescope elevation was changed in order to increase the sky coverage (Crill et al. 2003). The survey region aimed at CMB observations is $\sim 3\%$ of the sky or ~ 1200 square degrees (Ruhl et al. 2003). The data were obtained using 16 spiderweb bolometric detectors sensitive to four frequency bands centered at 90, 150, 240 and 410 GHz. Here we restrict ourselves to the 150 GHz data that have the most advantageous combination of sensitivity and angular resolution to target the CMB fluctuations. The analysis of B98 dataset produced the first high signal to noise CMB maps at subdegree resolution and one of the first high confidence measurements of the first acoustic peak in the CMB anisotropy angular spectrum (de Bernardis et al. 2000). The Gaussianity of this dataset has been constrained in both pixel and harmonic space (Polenta et al. 2002; De Troia et al. 2003).

The B03 experiment has been flown from Antarctica in 2003. Contrarily to B98, B03 was capable of measuring linear polarization other than total intensity (Piacentini et al. 2006; Montroy et al. 2006; Jones et al. 2006; MacTavish et al. 2006). It has observed the microwave sky for ~ 7 days in three frequency bands, centered at 145, 245 and 345 GHz. Here we use only the 145 GHz data, for reasons analogous to B98. These have been gathered with polarization sensitive bolometers (PSB), i.e. bolometers sensitive to total intensity and a combination of the two Stokes linear polarization parameters Q and U (Jones et al. 2002). The analysis of the dataset has produced high quality maps (Masi et al. 2006) of the southern sky that have been conveniently divided in three regions: a "deep" (in terms of integration time per pixel) survey region (~ 90 square degrees) and a "shallow" survey region (~ 750 square degrees), both at high Galactic latitudes, as well as a region of ~ 300 square degrees across the Galactic plane. The deep region is completely embedded in the shallow region.

[1] http://www.rssd.esa.int/index.php?project=planck

In this paper we apply a pixel mask to select a larger effective sky region than the one used in De Troia et al. (2007). We have been extremely careful in choosing this sky cut, rejecting regions potentially contaminated by foreground emission, which shows up clearly in the B98 higher frequency maps, and pixels falling too close to the edge of the survey region, which exhibit low signal to noise and potential visual artefacts. The final cut we use covers about 980 square degrees or 2.4% of the sky. This should be compared with the ~ 700 (1.7% of the sky) employed for De Troia et al. (2007), which only used B03, and with the 1.2% and 1.8% of the sky selected respectively for the B98 analyses of Polenta et al. (2002) and De Troia et al. (2003). The sky mask employed in this paper is the largest ever used for BOOMERanG non-Gaussianity studies.

We analysed the temperature (T) data map reduced jointly from eight PSB at 145 GHz (Masi et al. 2006) for the B03 dataset and the T map obtained from the best three of the six 150 GHz channels for B98. While we do not consider here the Stokes Q and U polarization maps, the B03 temperature map has been marginalized with respect to linear polarization. The maps have been produced with ROMA, an iterative generalized least square (GLS) map making code specifically tuned for BOOMERanG analysis (Natoli et al. 2001; De Gasperis et al. 2005). To work, the GLS map maker needs to know the detectors' noise power spectral densities, which is estimated directly from flight data using an iterative procedure. In the case of B03, where cross-talks among PSB located in the same feed horn are significant, we have also estimated the corresponding noise cross-spectra (Masi et al. 2006). The timelines have been carefully flagged to exclude unwanted data; for B98, only the more conservative part of the scan surveyed at 1 degree per second (d.p.s.) is used (Crill et al. 2003) while for both datasets we have flagged all of the turn-around data. Once the B98 and B03 maps are produced, we obtain a single data map by noise weighting the two. In doing so we treat the residual noise left in the map as white. This choice is motivated by a property of the GLS map making procedure, which is very effective in suppressing the level of noise correlations in the data. The noise level in the B98 map roughly equals that in the B03 shallow region: at $6.7'$ the noise r.m.s. is about 40 μK per pixel. (While the B98 flight actually lasted longer than B03, we consider only three channels and the 1 d.p.s. part of the scan here.) The noise r.m.s. in the B03 deep region is $\sim 10\mu$K for $6.7'$ pixels. The joint B03/B98 map we obtain is shown in Fig. 1, in the sky cut employed for the analysis hereafter.

To probe CMB non-Gaussianity it is important to keep under control contaminations from astrophysical foregrounds, whose pattern is markedly non-Gaussian. In the region selected here, foreground intensity is known to be negligible with respect to the cosmological signal (Masi et al. 2006). We have masked all detectable sources in the observed field. To assess the robustness of our tests of Gaussianity we used a set of 1000 Monte Carlo simulation maps that mimic both the B03 and the B98 data. To produce these simulations, the following scheme is employed. The Gaussian CMB sky signal is simulated using the cosmological parameters estimated from the WMAP 1-year data (Hinshaw et al. 2003) which fits well the BOOMERanG temperature power spectrum. This signal is smoothed according to the measured optical beam and synthesized into a pixelized sky map, using HEALPix routines (Górski et al. 2005). Taking into account the B03 and B98 scanning strategy, the signal map is projected onto eight timestreams, one for each 145 GHz detector, for B03 and onto three timestreams for the B98 150 GHz channels we consider here. Noise only timestreams are also produced, as Gaussian realizations of each detector's noise power spectral density, iteratively estimated from flight data as explained above, taking into account cross talks between detectors in the case of B03. The signal and noise timelines are then added together. To reduce the simulated timelines, we follow the same steps performed when analysing real data: the timelines are then reduced with the ROMA mapmaking code replicating the actual flight pointing and transient flagging, to produce T maps jointly from three B98 channels and T, Q and U maps jointly from all eight B03 channels. We enforce that the map making procedure is applied to simulation and observational data following the same steps.

It is worth noticing that in this paper the B98 and B03 data have been used to produce a joint map for the first time.

3 PERTURBATIVE APPROACH TO MINKOWSKI FUNCTIONAL FOR A WEAKLY NON-GAUSSIAN CMB FIELD

In the previous paper (De Troia et al. 2007) we have also applied simple pixel based analysis (specifically, the normalized skewness and kurtosis) to the B03 observed field. Here we restrict ourselves to three Minkowski Functionals generally defined in two-dimensional maps: fraction of area V_0, total circumference V_1, and Euler Characteristic V_2. We measure the MFs for CMB temperature maps above the threshold density ν, defined as the temperature fluctuation $f \equiv \Delta T/T$ normalized by its standard deviation $\sigma \equiv \langle f^2 \rangle^{1/2}$. Following the formalism by Matsubara (2003) and Hikage et al. (2006), we can write the analytical formula for the k-th Minkowski functional of weakly non-Gaussian fields as

$$V_k(\nu) = \frac{1}{(2\pi)^{(k+1)/2}} \frac{\omega_2}{\omega_{2-k}\omega_k} \left(\frac{\sigma_1}{\sqrt{2}\sigma_0}\right)^k e^{-\nu^2/2} \left\{ H_{k-1}(\nu) + \left[\frac{1}{6} S^{(0)} H_{k+2}(\nu) + \frac{k}{3} S^{(1)} H_k(\nu) + \frac{k(k-1)}{6} S^{(2)} H_{k-2}(\nu) \right] \sigma_0 + \mathbf{O}(\sigma_0^2) \right\}, \quad (2)$$

where $H_n(\nu)$ are the Hermite polynomials and $\omega_k = \pi^{k/2}\Gamma(k/2+1)$ gives $\omega_0 = 1$, $\omega_1 = 2$, and $\omega_2 = \pi$. The $S^{(i)} (i = 0, 1, 2)$ are skewness parameters, defined by

$$S^{(0)} \equiv \frac{\langle f^3 \rangle}{\sigma_0^4}, \quad (3)$$

$$S^{(1)} \equiv -\frac{3}{4} \frac{\langle f^2 (\nabla^2 f) \rangle}{\sigma_0^2 \sigma_1^2}, \quad (4)$$

$$S^{(2)} \equiv -3 \frac{\langle (\nabla f) \cdot (\nabla f) (\nabla^2 f) \rangle}{\sigma_1^4}. \quad (5)$$

The variances $\sigma_j^2 (j = 0, 1)$ are calculated from C_ℓ as

$$\sigma_j^2 \equiv \frac{1}{4\pi} \sum_\ell (2\ell + 1) \left[\ell(\ell+1)\right]^j C_\ell W_\ell^2, \quad (6)$$

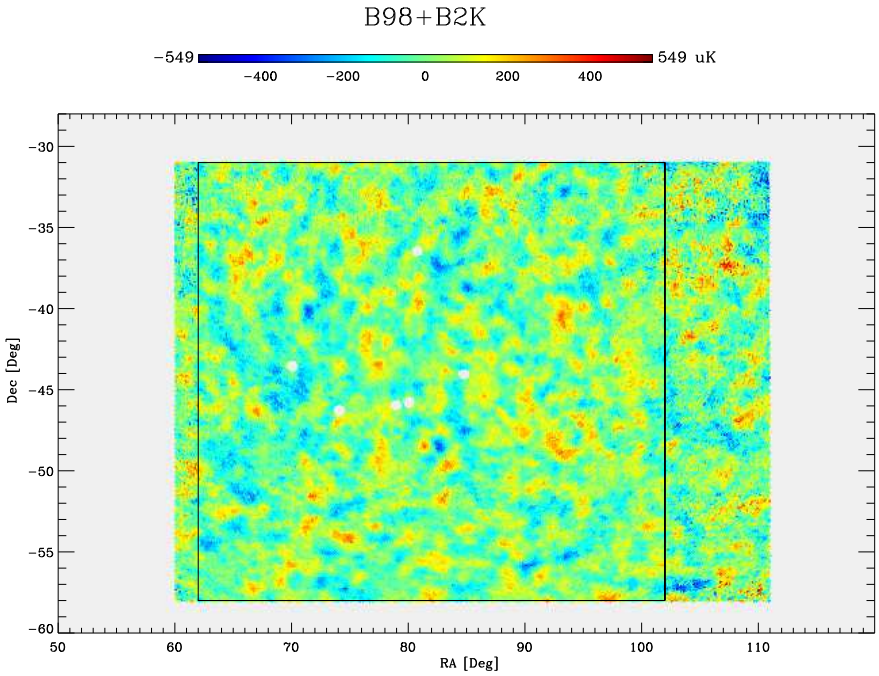

Figure 1. The CMB field as seen in the B2K + B98 map, in the sky cut used for the analysis presented here. The solid line shows the boundary of the region taken in consideration for the analysis in De Troia et al. (2007).

where W_ℓ is a window function that includes the experiment's effective optical transfer function (assumed circularly symmetric) and low-ℓ and high-ℓ cut-off as well as the filter function due to pixelization effects. Expanding the skewness parameters into spherical harmonics and using the reduced bispectrum $b_{\ell_1\ell_2\ell_3}$ as a function of $f_{\rm NL}$ (Komatsu & Spergel 2001), we get:

$$S^{(0)} = \frac{3}{2\pi\sigma_0^4}\sum_{2\leqslant\ell_1\leqslant\ell_2\leqslant\ell_3} I^2_{\ell_1\ell_2\ell_3} b_{\ell_1\ell_2\ell_3} W_{\ell_1} W_{\ell_2} W_{\ell_3}, \quad (7)$$

$$S^{(1)} = \frac{3}{8\pi\sigma_0^2\sigma_1^2}\sum_{2\leqslant\ell_1\leqslant\ell_2\leqslant\ell_3} [\ell_1(\ell_1+1)+\ell_2(\ell_2+1) \quad (8)$$
$$+\ell_3(\ell_3+1)] I^2_{\ell_1\ell_2\ell_3} b_{\ell_1\ell_2\ell_3} W_{\ell_1} W_{\ell_2} W_{\ell_3},$$

$$S^{(2)} = \frac{3}{4\pi\sigma_1^4}\sum_{2\leqslant\ell_1\leqslant\ell_2\leqslant\ell_3} \{[\ell_1(\ell_1+1)+\ell_2(\ell_2+1)$$
$$-\ell_3(\ell_3+1)]\ell_3(\ell_3+1)+(\text{cyc.})\} \quad (9)$$
$$\times I^2_{\ell_1\ell_2\ell_3} b_{\ell_1\ell_2\ell_3} W_{\ell_1} W_{\ell_2} W_{\ell_3}, \quad (10)$$

where

$$I_{l_1 l_2 l_3} \equiv \sqrt{\frac{(2l_1+1)(2l_2+1)(2l_3+1)}{4\pi}} \begin{pmatrix} l_1 & l_2 & l_3 \\ 0 & 0 & 0 \end{pmatrix}. \quad (11)$$

In the above theoretical predictions we assume a ΛCDM model with the cosmological parameters at the maximum likelihood peak from WMAP 1-year data (Spergel et al. 2003): $\Omega_{\rm b} = 0.043$, $\Omega_{\rm cdm} = 0.21$, $\Omega_\Lambda = 0.74$, $H_0 = 72$km s^{-1} Mpc^{-1}, $n_{\rm s} = 0.96$, and $\tau = 0.11$. The amplitude of primordial fluctuations has been normalized to the first peak amplitude of the temperature power spectrum, $\ell(\ell+1)C_\ell/(2\pi) = (74.7\mu{\rm K})^2$ at $\ell = 220$ (Page et al. 2003).

We compute the MFs of the pixelized maps by integrating a combination of first and second angular derivatives of the temperature over the sky, as described in Appendix A.1. of Hikage et al. (2006). The threshold density ν is set in the range -3.6 to 3.6, assuming 19 evenly spaced grid points. For our analysis we use maps at HEALPix (Górski et al. 2005) resolution of $\sim 13'$ ($N_{\rm side} = 256$) and $\sim 7'$ ($N_{\rm nside} = 512$).

4 CONSTRAINTS ON PRIMORDIAL NON-GAUSSIANITY

We define a "joint" estimator by grouping the V_k's in a single, 57 elements data vector $V_J \equiv \{V_0(\nu=-3.6), V_0(\nu=-3.2), ..., V_0(\nu=3.6), V_1(\nu=-3.6), ..., V_2(\nu=3.6)\}$. We want now to constrain the $f_{\rm NL}$ parameter and estimate its best fit value. Starting from analytical formulae we can calculate the non-Gaussian part of the MFs using the equation (2), i.e.:

$$\Delta V_J(f_{\rm NL}) = V_J(f_{\rm NL}) - V_J(f_{\rm NL}=0). \quad (12)$$

We can then estimate our final non-Gaussian predictions as:

$$\tilde{V}_J(f_{\rm NL}) = \bar{V}_J(f_{\rm NL}=0) + \Delta V_J(f_{\rm NL}), \quad (13)$$

where $\bar{V}_J(f_{\rm NL}=0)$ is the average MF computed from our Gaussian Monte Carlo simulations. The reason for this choice is that the Monte Carlo average provides an accurate estimate of the MFs, accounting for instrumental and coverage effect. Finally we perform a chi-square analysis by

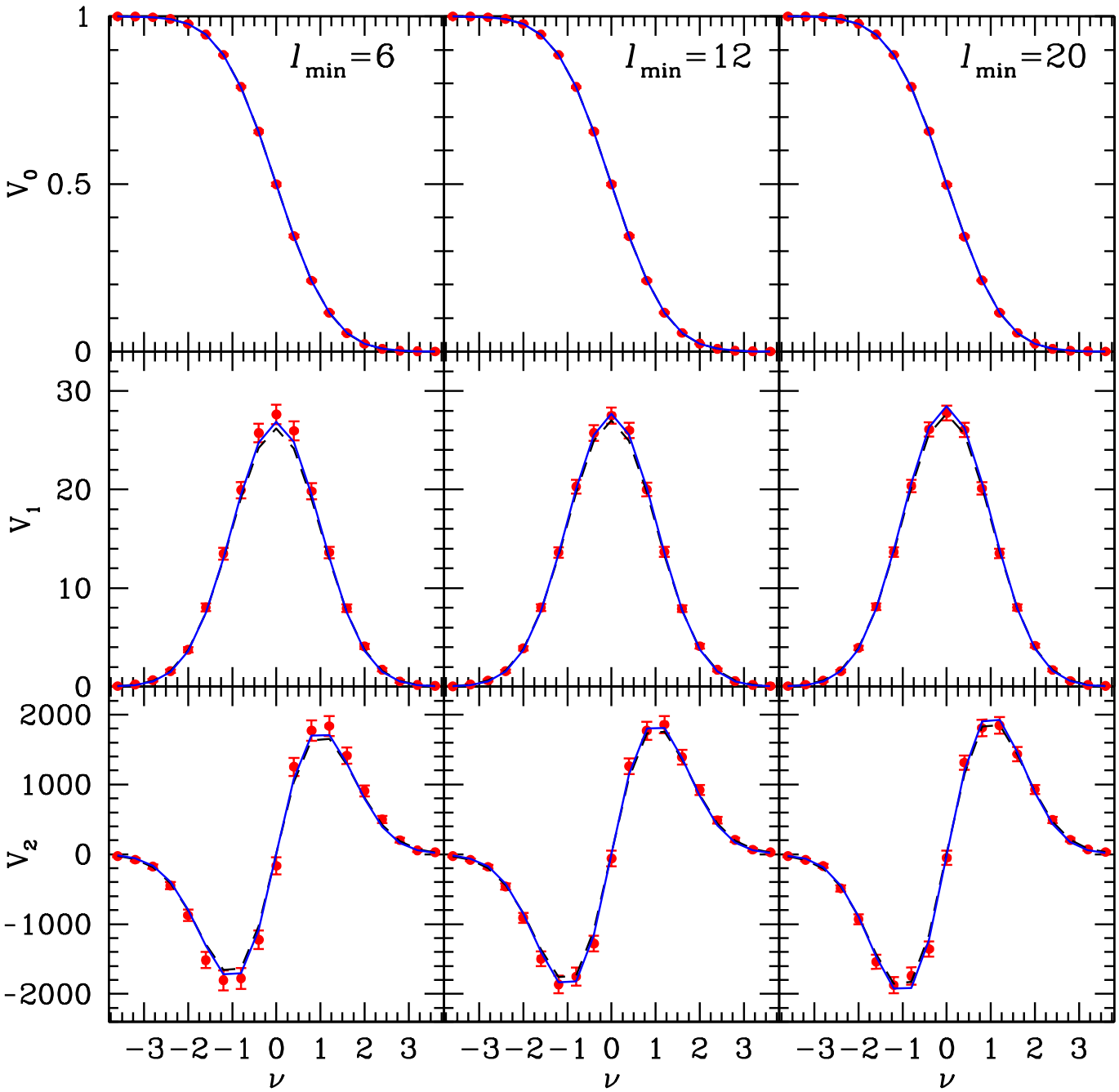

Figure 2. The plots show, from top to bottom, V_0, V_1 and V_2 computed from the BOOMERanG data (filled circles), from analytical formulae (solid line, here computed with the best fit $f_{\rm NL}$ value for each functional) and from Gaussian Monte Carlo simulations (dashed lines). The columns refer to different choices of the low ℓ cut (see text), $\ell_{\rm min} = 6$, 12 and 20 (from left to right). The error-bars for the data are derived as the 1-σ standard deviation of our Monte Carlo simulations. The pixel size of the map is $\sim 7'$ (HEALPix $N_{\rm side} = 512$).

measuring

$$\chi^2 = \sum_{JJ'} [V_J^{\rm B98+B03}(\nu) - \tilde{V}_J(f_{\rm NL})] C^{-1}_{J,J'} [V_{J'}^{\rm B98+B03} - \tilde{V}_{J'}(f_{\rm NL})], \quad (14)$$

where $V_J^{\rm B98+B03}$ denote the MFs for the joint B98 and B03 map. This expression is used to derive constraints for $f_{\rm NL}$ and for our goodness of fit analysis. The full covariance matrix $C_{J,J'}$ is also estimated from Gaussian Monte Carlo simulations. We have verified that, when computing its matrix elements, one needs to take into account the correlations among different functionals not to incur in biased constraints. In Fig. 2 we plot each MF of the B98 and B03 data compared with the theoretical predictions with the best fit value of $f_{\rm NL}$ for each MF. The error-bars are derived as 1-σ deviations estimated from 1000 Gaussian maps with correlated noise.

We study the effect that neglecting the contribution of

a range of multipoles ℓ has on this analysis. A low ℓ cut is necessary since we are dealing with data from a suborbital experiment, which has not been designed to measure large angular scales. These cannot be constrained properly, firstly because of the limited angular extension of the region surveyed, and secondly because timeline filtering is applied to the data to suppress contribution from low frequency noise and systematics. The filters are applied during the map making stage at ~ 70 mHz both for B03 and for B98 (Masi et al. 2006; Crill et al. 2003). While we apply the same filters in our simulations, the amount of low ℓ power in the latter is somewhat different from those exhibited by the data. This happens because the GLS map maker is more efficient in recovering the large scale structure from the simulations, where we only add Gaussian noise with random phases, than from the data where the noise has a more complex structure. To account for this effect, we exploit one degree of freedom allowed by the harmonic analysis to MF here pursued: specifically, we set to zero all the power in the map below $\ell_{\rm min}$. The left to right panels of Fig. 2 refer to three different choices: $\ell_{\rm min}$ =6, 12 and 20 respectively. The $\ell_{\rm min} = 6$ cut is the natural one that would arise due to limited sky coverage but in this case the MFs from data and simulations do not agree well for V_1 and V_2 (see Fig 2). The agreement is much better for $\ell_{\rm min} = 12$ and $\ell_{\rm min} = 20$ with no appreciable difference between the two. This comes with little surprise, since a telescope scan speed in the range 0.5°/s to 1°/s, both of which have been employed in the dataset we consider, effectively high pass filters the data in the range $10 \lesssim \ell \lesssim 20$. (Note, however, that timeline filtering has an anisotropic effect on the sky, due to the nature of the scanning strategy employed for BOOMERanG.)

On the other hand, it is advantageous to consider also a high ℓ cut $\ell_{\rm max}$ to probe how the decreasing signal to noise level can affect $f_{\rm NL}$ constraints. For the data, this can be done by varying the HEALPix resolution parameter $N_{\rm side}$ which is linked to $\ell_{\rm max}$ in the spherical harmonic transform. We focus in the following on both $N_{\rm side} = 256$ with $\ell_{\rm max} = 512$ and $N_{\rm side} = 512$ with $\ell_{\rm max} = 1000$. Our dataset is signal dominated at $\ell \simeq 500$ while begins to be noise dominated at $\ell \simeq 1000$ (Jones et al. 2006).

In Fig. 3 we show the analytical non-Gaussian corrections ΔV_J (eq.[12]) for each MF compared to the residuals obtained by subtracting to the B98/B03 data MFs their Monte Carlo average, that is, $V_J^{\rm B98+B03} - \bar{V}_J(f_{\rm NL} = 0)$. The error-bars represent the 1σ error estimated from 1000 Gaussian Monte Carlo simulations. The analytical residuals are computed using the best fit value of $f_{\rm NL}$ as obtained by minimizing the χ^2 in the equation (14), albeit this is done separately for each MF, ignoring (only for the sake of this plot) correlations among different functionals. The analytical ΔV_J in Fig. 3 are normalized to the maximum of their Gaussian part, while the data points are normalized to the maximum of the Monte Carlo average. We show results both for $N_{\rm side} = 256$ (left) and for $N_{\rm side} = 512$ (right) and for a low-multiple cut at $\ell_{\rm min} = 6$, 12 and 20 (left to right). The agreement of the residual plots suggests that it is safer to adopt the most conservative cut at $\ell_{\rm min} = 20$. Since increasing further the cut does not appear to yield further advantage, we focus on a conservative choice $\ell_{\rm min} = 20$ for our final analysis.

Table 1 lists the confidence intervals for $f_{\rm NL}$ estimated from the BOOMERanG data at different $\ell_{\rm min}$ and $\ell_{\rm max}$ thresholds. The results are obtained taking into account the full covariance matrix of the V_k's, as expressed in the equation (14) above. The MFs computed at different HEALPix resolution encode different statistical information on the underlying field and thereby combining two sets of MFs improve the limits on $f_{\rm NL}$. We build a global covariance matrix to take also into account correlations among the two sets. We repeat this process for each $\ell_{\rm min}$ value considered.

In the conservative case of $\ell_{\rm min} = 20$ using the "combined" estimator, our χ^2 analysis yields $-670 < f_{\rm NL} < 30$ at 1-σ level and $-1020 < f_{\rm NL} < 390$ at 95% CL, while the minimum (best fit) value of $f_{\rm NL}$ is at -320. The previous analysis performed only on the B03 dataset (De Troia et al. 2007) produced limits weaker than those obtained in this paper by a factor $\simeq 1.4$. The improvement is due to a combination of both enhanced sky coverage and the use of the analytical estimator. The B98 dataset alone has never been subject so far to $f_{\rm NL}$ analysis. We have checked that this dataset too is compatible with $f_{\rm NL} = 0$ at 1-σ with $\Delta f_{\rm NL} = 470$ ($\Delta f_{\rm NL} = 930$ at 2-σ).

We can also quantify the cost of imposing a low ℓ cut to the data. In fact, had we not considered an effective $\ell_{\rm min}$ value, one would expect to reduce the confidence interval on $f_{\rm NL}$ by $\simeq 1.6$ (c.f. the last row in Table 1, obviously obtained not from the data but from a simulation containing a low resolution pattern). In practice, this could be obtained by adding to the dataset a low resolution CMB field coming, e.g., from the WMAP data. While this would give us tighter constraints on $f_{\rm NL}$, we prefer to focus here on the limits one can derive from the BOOMERanG data alone. Note also, that a diminished sensitivity to low resolution features is a characteristic common to most -if not all- of the suborbital experiments. The accurate measurement of the CMB at low and high multipoles with one single experiment is rather a prerogative of space born missions, which enjoy the necessary stability and long term integration capability. Our analysis is the first (to our knowledge) to explicitly take into account this effect for a suborbital experiment. To explain the significant broadening of $f_{\rm NL}$ constraints caused by the low ℓ cut, one can note that for the underlying ("local") form of non-Gaussianity we are probing here, the low multipoles are actually very important. In fact, most of the signal in the reduced bispectrum $b_{\ell_1\ell_2\ell_3}$ lies in "squeezed" ℓ-space triangles, with one side much smaller than the other two. When probing non-Gaussianity one is basically comparing signal at the lowest multipole with two of the highest multipoles. As a result, S/N increases as $\ell_{\rm max}/\ell_{\rm min}$ so one can either increase $\ell_{\rm max}$ for a given $\ell_{\rm min}$ (which explains, e.g., the improvement of WMAP over COBE and the forecasted improvement of PLANCK over WMAP), or reducing $\ell_{\rm min}$ for a given $\ell_{\rm max}$.

5 CONCLUSIONS

We have analysed data from the BOOMERanG experiment, combining for the first time the temperature maps of the 1998 and 2003 campaigns, to constrain a non-Gaussian primordial component in the observed CMB field. We focused on Minkowski Functionals, comparing the data to analytical perturbative corrections in order to get constraints on the

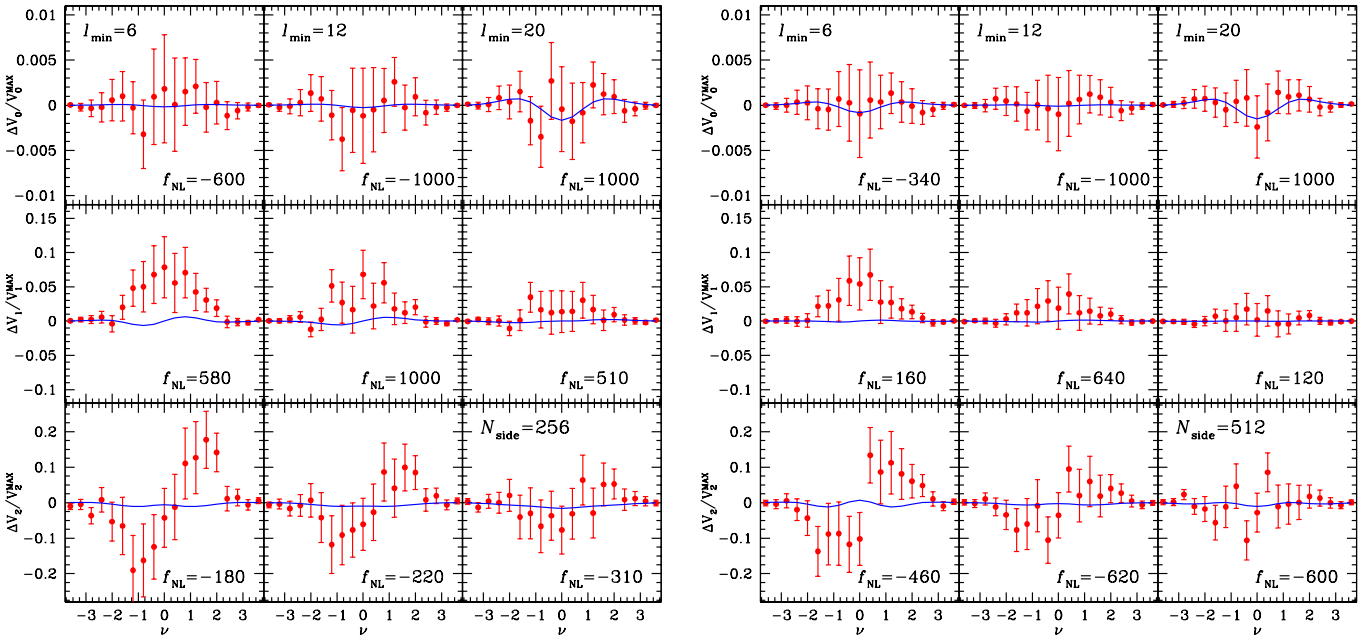

Figure 3. Comparison of the three MFs residuals for B98/B03 temperature data (filled circles) to the analytical predictions with the best fit value of $f_{\rm NL}$ for each functional (solid lines). The analytical predictions are normalized to the maximum value of the Gaussian part while the data points are normalized to the maximum of the Monte Carlo average. The left figure is for HEALPix $N_{\rm side} = 256$ resolution while the right figure is for $N_{\rm side} = 512$. From left to right in each figure, we show the $\ell_{\rm min} = 6$, 12 and 20 cases. The error-bars represent the standard deviation at 1-σ estimated from 1000 Gaussian Monte Carlo simulations.

$\ell_{\rm min}$	$\ell_{\rm max} = 512$		$\ell_{\rm max} = 1000$		Combined	
	1σ	2σ	1σ	2σ	1σ	2σ
6	340	660	790	1570	320	620
12	360	710	970	1930	350	690
20	380	730	910	1830	360	730
2	260	510	470	920	260	510

Table 1. The confidence intervals for $f_{\rm NL}$ estimated for the B03/B98 data with different low and high ℓ cut values (see text). We show both the 1σ and 2σ confidence interval. The last two columns are obtained from a combined analysis of data for the two $\ell_{\rm max}$ values. The last row is derived using a simulation with no effective low ℓ cut and shows the improvement that could be obtained if a low resolution pattern had been present in the BOOMERanG field.

non-linear coupling parameter $f_{\rm NL}$. We have used a set of highly realistic simulation maps of the observed field generated assuming a Gaussian CMB sky, since the formalism we have adopted does not require non-Gaussian simulation maps. We studied the effect that the lack of low resolution CMB features in the BOOMERanG data has on $f_{\rm NL}$ constraints. We find $-670 < f_{\rm NL} < 30$ at 68% CL and $-1020 < f_{\rm NL} < 390$ at 95% CL. These limits are significantly better than those published in a previous analysis limited to the BOOOMERanG 2003 data ($-800 < f_{\rm NL} < 1050$ at 95% CL), represent the best results to date for suborbital experiments and probe angular scales smaller than those accessible to the WMAP.

ACKNOWLEDGMENTS

The BOOMERanG team gratefully acknowledge support from the CIAR, CSA, and NSERC in Canada; Agenzia Spaziale Italiana, University La Sapienza and Programma Nazionale Ricerche in Antartide in Italy; PPARC and the Leverhulme Trust in the UK; and NASA (awards NAG5-9251 and NAG5-12723) and NSF (awards OPP-9980654 and OPP-0407592) in the USA. Additional support for detector development was provided by CIT and JPL. Field, logistical, and flight support were supplied by USAP and NSBF; This research used resources at NERSC, supported by the DOE under Contract No. DE-AC03-76SF00098, and at CASPUR (Rome, Italy: special thanks are due to M. Botti and F. Massaioli). We also acknowledge partial support from ASI Contract I/016/07/0 "COFIS" and ASI Contract Planck LFI activity of Phase E2. Some of the results in this paper have been derived using the HEALPix package (Górski et al. 2005). C. H. acknowledges support from the Particle Physics and Astronomy Research Council grant number PP/C501692/1 and a JSPS (Japan Society for the Promotion of Science) fellowship.

REFERENCES

Bartolo N., Komatsu E., Matarrese S., Riotto A., 2004, Phys. Rept., 402, 103
Bernardeau F., Uzan J.-F., 2002, Phys. Rev. D, 66, 103506
Creminelli P., Senatore L., Zaldarriaga M., Tegmark M. 2007, JCAP, 3, 5
Crill B. P. et al., 2003, ApJS, 148, 527
Cruz M., Cayón L., Martínez-González E., Vielva P., Jin J., 2007, ApJ, 655, 11

Curto A., Macías-Pérez J. F., Martínez-González E., Barreiro R. B., Santos D., Hansen F. K., Liguori M., Matarrese S., 2008, A&A, 486, 383
Curto A., Martínez-González E., Barreiro R. B., preprint (arXiv:0902.1523)
de Bernardis P. et al., 2000, Nature, 404, 955
de Gasperis G. et al., 2005, A&A, 436, 1159
De Troia G. et al., 2007, ApJ, 670, L73
De Troia G., et al., 2003, MNRAS, 343, 284
Eriksen H. K., Banday A. J., Górski K. M., Hansen F. K., Lilje P. B., 2007, ApJ, 660, L81
Gangui A., Lucchin F., Matarrese S., Mollerach S., 1994, ApJ, 430, 447
Górski K. M. et al., 2005, ApJ, 622, 759
Hikage C., Komatsu E., & Matsubara T., 2006, ApJ, 653, 11
Hikage, C., Matsubara, T., Coles, P., Liguori, M., Hansen, F. K., Matarrese, S., 2008, MNRAS, 389, 1439
Hinshaw G. et al., 2003, ApJS, 148, 135
Komatsu E., Spergel D. N., 2001, Phys. Rev. D, 63, 063002
Komatsu E. et al., 2009, ApJS, 180, 330
Jones W. C. et. al., 2006, ApJ. 647, 823
Jones W. C., Bhatia R. S., Bock J. J., Lange A. E., SPIE Proceedings, Waikaloa, 2002, preprint (astro-ph/0209132)
Lyth D. H., Ungarelli C., Wands D., 2003, Phys. Rev. D, 67, 23503
MacTavish C. J. et al., 2006, ApJ, 647, 799
Matsubara T. 2003, ApJ, 584, 1
Masi S. et al., 2006, A&A, 458, 687
Montroy T. E. et al., 2006, ApJ, 647, 813
Natoli P. et al., 2001, A&A, 371, 346
Page L. et al., 2003, ApJS, 148, 39
Park C.-G., Park C., Gott III J. R., 2007, ApJ, 660, 959
Piacentini F. et al., 2006, ApJ, 647, 833
Pietrobon D., Cabella P., Balbi A., de Gasperis G., Vittorio N., 2009, MNRAS, 682
Polenta G. et al., 2002, ApJ, 572, L27
Räth C., Morfill G. E., Rossmanith G., Banday A. J., Górski K. M., 2009, Phys. Rev. Lett., 102, 131301
Rudjord O., Hansen F. K., Lan X., Liguori M., Marinucci D., Matarrese S., 2009, preprint (arXiv:0901.3154)
Ruhl J. E. et al., 2003, ApJ, 599, 786
Salopek D. S., Bond J. R., 1990, Phys. Rev. D, 42, 3936
Santos M. G. et al., 2003, MNRAS, 341, 623
Smith K. M., Senatore L., Zaldarriaga M., 2009, preprint (arXiv:0901.2572)
Smith S. et al., 2004, MNRAS, 352, 887
Spergel D. et al., 2003, ApJS, 148, 175
Verde L., Wang L., Heavens A. F., Kamionkowski M., 2000, MNRAS, 313, 141
Vielva P., Martínez-González E., Barreiro R. B., Sanz J. L., Cayón L., 2004, ApJ, 609, 22
Yadav A. P. S., Wandelt B., D., 2008, Phys. Rev. Lett., 100, 181301